nature portfolio

https://doi.org/10.1038/s41560-022-00988-w

Supplementary information

Ta–TiO_x nanoparticles as radical scavengers to improve the durability of Fe–N–C oxygen reduction catalysts

In the format provided by the authors and unedited

Supporting Information for

Ta-TiO_x Nanoparticles as Radical Scavengers to Improve the Durability of Fe-N-C Oxygen Reduction Catalysts

Hua Xie,[1a] Xiaohong Xie,[2a] Guoxiang Hu,[3*] Sulay Saha,[4] Lorelis Gonzalez-Lopez,[1] Venkateshkumar Prabhakaran,[2] Abhijit Phakatkar,[5] Min Hong,[1] Meiling Wu,[1] Reza Shahbazian-Yassar,[5*] Vijay Ramani,[4] Mohamad I. Al-Sheikhly,[1] De-en Jiang,[6] Yuyan Shao,[2*] Liangbing Hu[1*]

1. Department of Materials Science and Engineering, University of Maryland, College Park, Maryland, 20742, USA
2. Pacific Northwest National Laboratory, Richland, Washington, 99352, USA
3. Department of Chemistry and Biochemistry, Queens College of the City University of New York, Queens, NY 11367, USA
4. Center for Solar Energy and Energy Storage and Department of Energy, Environmental and Chemical Engineering, Washington University in St. Louis, St. Louis, Missouri 63130, USA
5. Department of Mechanical and Industrial Engineering, University of Illinois at Chicago, Chicago, Illinois 60607, USA
6. Department of Chemistry, University of California, Riverside, California 92521, USA

Supplementary Discussion

EPR theoretical background

Attack from $^{\bullet}OH$ and $HO_2^{\bullet}$ radicals and H_2O_2 is considered one of the most critical sources of degradation of PGM-free oxygen reduction catalysts. These oxidizing species are produced from the emerging electrons from the cathodes to the water according to the following reactions:
Since the $[H_3O^+]$ at pH ~0.0 is extremely high, ~ 1 M, the released electrons from the cathode react directly with H_3O^+ at the cathode surface to produce H-atoms. The latter react with the dissolved oxygen very rapidly to produce $HO_2^{\bullet}$,

$$e^- \text{ or } e_{aq}^- + H_3O^+ \rightarrow H + H_2O \qquad (1)$$

The reaction rate constant $k_1 = 2.3 \times 10^{10}$ $Lmol^{-1}s^{-1}$

then:

$$H + O_2 \rightarrow HO_2^{\bullet} \qquad (2)$$

The reaction rate constant $k_2 = 2.1 \times 10^{10}$ $Lmol^{-1}s^{-1}$

These two reactions are diffusion-controlled and take place within several nanoseconds. Also, the released electrons react very rapidly with the dissolved oxygen at the cathode surface to produce the superoxide anions according to the following reaction:[1]

$$e_{aq}^- + O_{2.} \rightarrow O_2^{\bullet -} \qquad (3)$$

The reaction rate constant $k_3 = 1.9 \times 10^{10}$ $Lmol^{-1}s^{-1}$

Equation 3 is a diffusion-controlled reaction and takes place within several nanoseconds. The continuous production of superoxide $O_2^{\bullet -}$ leads to the formation of H_2O_2 according to the following fast reaction:

$$2\ O_2^{\bullet -} \xrightarrow{H_2O} H_2O_2 + O_2 + 2OH^- + H_2O_{2.} \qquad (4)$$

The reaction rate constant $k = 1.5 \times 10^7$ $Lmol^{-1}$ s^{-1} and this reaction proceeds much faster under acidic media[2].

However, under our experimental conditions, where the pH ~0.0, the $O_2^{\bullet-}$ converts very rapidly and directly to the oxidizing species of perhydroxyl radicals $HO_2^{\bullet}$. The produced $HO_2^{\bullet}$ from the above reactions undergoes a very fast bimolecular reaction to produce H_2O_2,

$$2\ HO_2^{\bullet} \rightarrow H_2O_2 + O_2. \qquad (5)$$

The rate constant k = 8.3 x 10^7 $Lmol^{-1}s^{-1}$

Under these experimental conditions, where $[H_3O^+]$ is very high, and $[O_2]$ is also relatively high, the reductive species of e^- or e_{aq}^- are converted to the oxidizing species, $HO_2^{\bullet}$ and H_2O_2. The unstable H_2O_2 decomposes readily to the powerful oxidizing radical of $^{\bullet}OH$ via the Fenton reaction as follows:

$$M^{n+} + H_2O_2 \rightarrow {}^{\bullet}OH + OH^- + M^{(n+1)+} \qquad (6)$$

$^{\bullet}OH$ radicals induce the rupture of the C-C bonds from PGM-free catalysts, leading to the formation of the C-centered radicals.[3] Molecular oxygen reacts very rapidly with the C-centered radicals to produce the corresponding peroxyl radicals ($R\text{-}C\text{-}O_2^{\bullet}$). These $R\text{-}C\text{-}O_2^{\bullet}$ radicals undergo various complicated reactions to form CO_2 and CO.

During the Fenton reaction, the hydroxyl radicals form via the following process:

$$Fe^{2+} + H_2O_2 \rightarrow Fe^{3+} + OH^- + {}^{\bullet}OH \qquad (7)$$

$$Fe^{2+} + {}^{\bullet}OH \rightarrow Fe^{3+} + OH^- \qquad (8)$$

$$^{\bullet}OH + H_2O_2 \rightarrow {}^{\bullet}OOH + H_2O \qquad (9)$$

$$^{\bullet}OH + {}^{\bullet}OH \rightarrow H_2O_2 \qquad (10)$$

When an excess of DMPO is present in the Fenton reaction solution, $^{\bullet}OH$ rapidly attacks DMPO (as shown below in Equation 11 to form the paramagnetic compound 2-hydroxy-5,5-dimethyl-1-pyrrolidinyloxy (OH-DMPO$^{\bullet}$).

$$DMPO + {}^{\bullet}OH \rightarrow OH - DMPO^{\bullet} \qquad (11)$$

Using the spin trapping technique, the short-lived hydroxyl (•OH) radical undergoes an addition reaction to the spin trap (DMPO), producing a relatively long-lived free radical product, i.e., the hydroxyl radical spin adduct (OH-DMPO•). With DMPO, the reaction can be represented as:

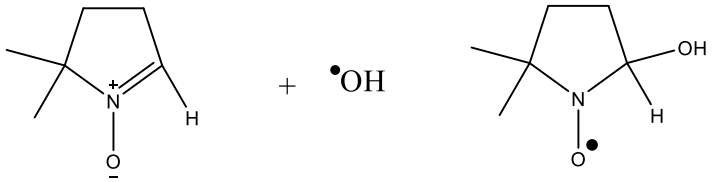

EPR is then used to identify and measure the concentration of this radical in the solution.

Supplementary Figures

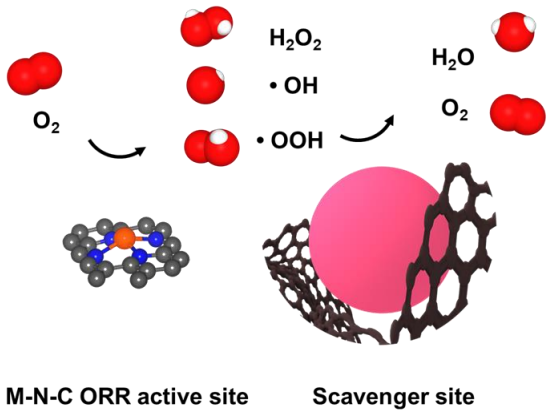

Supplementary Figure 1. Schematic of the fast removal of H_2O_2 and radicals by Ta-TiO_x nanoparticles.

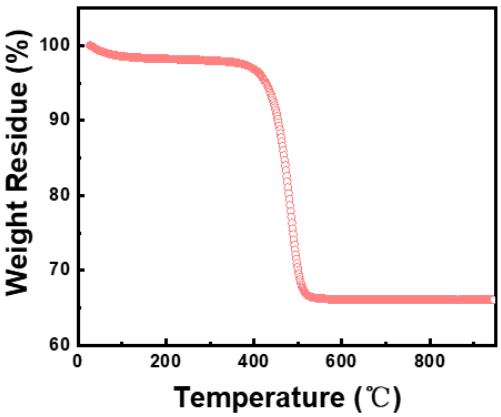

Supplementary Figure 2. Thermogravimetric analysis result of the Ta-TiO_x on Ketjenblack carbon in oxygen environment. When the temperature reaches 600 ^oC, the carbon becomes completely decomposed. The results show that the Ta-TiO_x nanoparticles account for 66 wt% of the total weight.

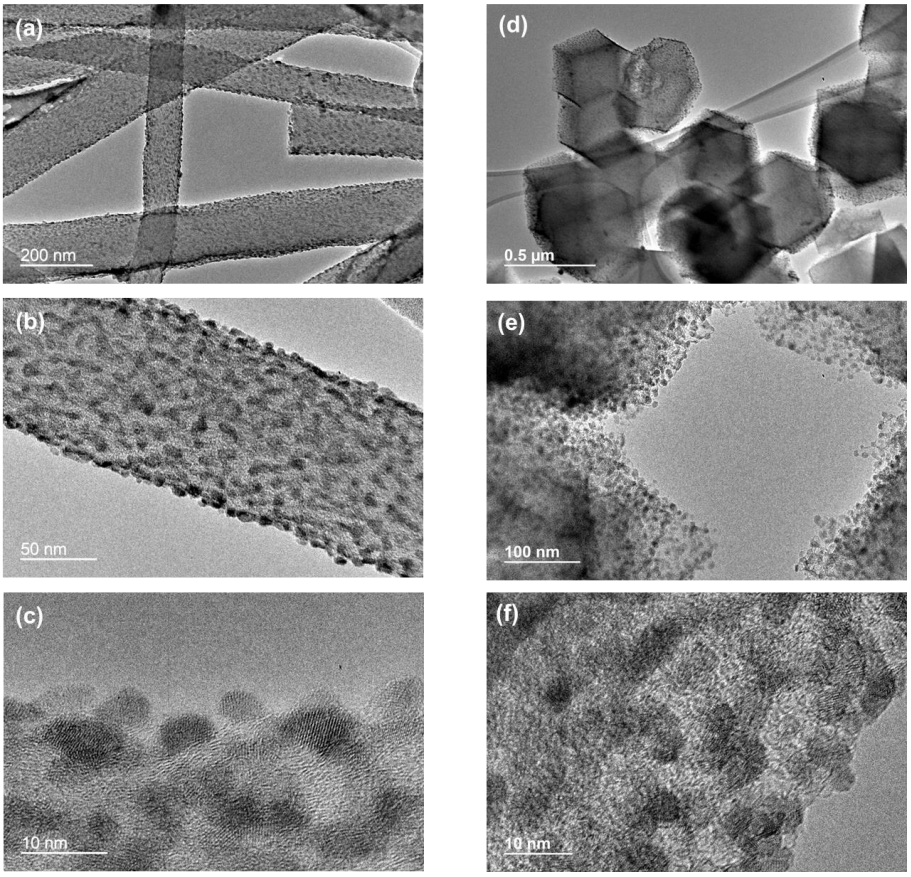

Supplementary Figure 3. The high-temperature pulse approach allows us to deposit Ta-TiO_x nanoparticles on various substrates, including (a)-(c) carbon nanofiber membranes and (d)-(f) carbon derived from the pyrolysis of metal–organic frameworks.

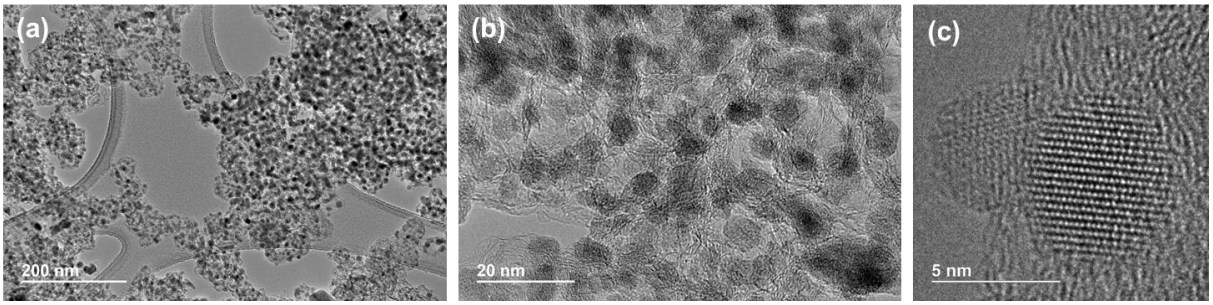

Supplementary Figure 4. TEM images at different magnifications of the Ta-TiO_x nanoparticles deposited on the Ketjenblack carbon substrate via the high-temperature pulse approach. The well-crystallized oxide nanoparticles are of a uniform size, evenly distributed across the substrate.

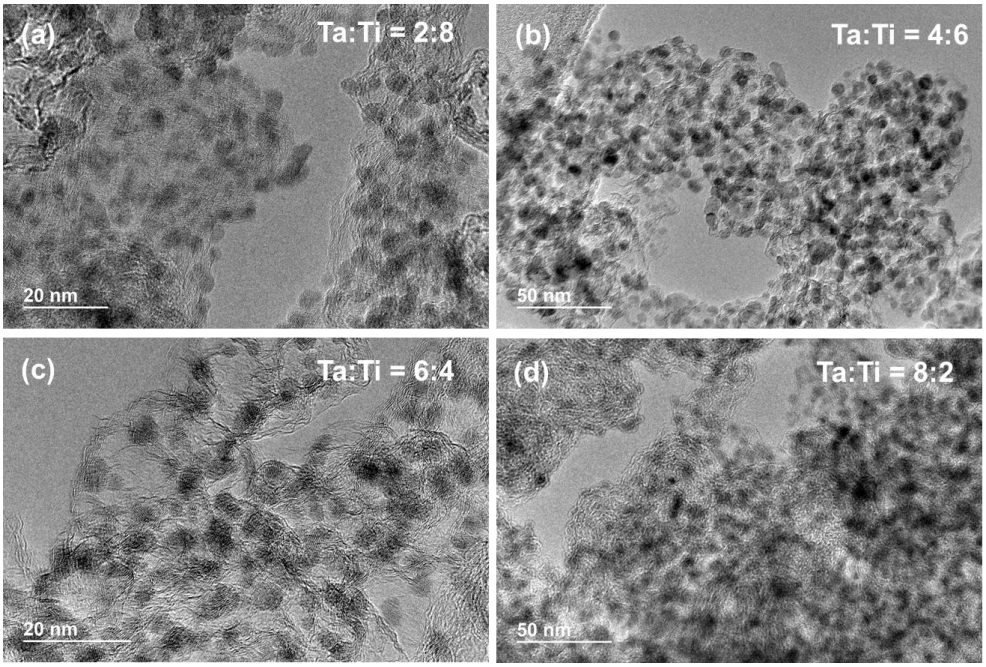

Supplementary Figure 5. TEM images of the Ta-TiO_x nanoparticles synthesized at different Ta/Ti ratios of (a) 2:8, (b) 4:6, (c) 6:4, and (d) 8:2. There was no obvious morphology change in the nanoparticles.

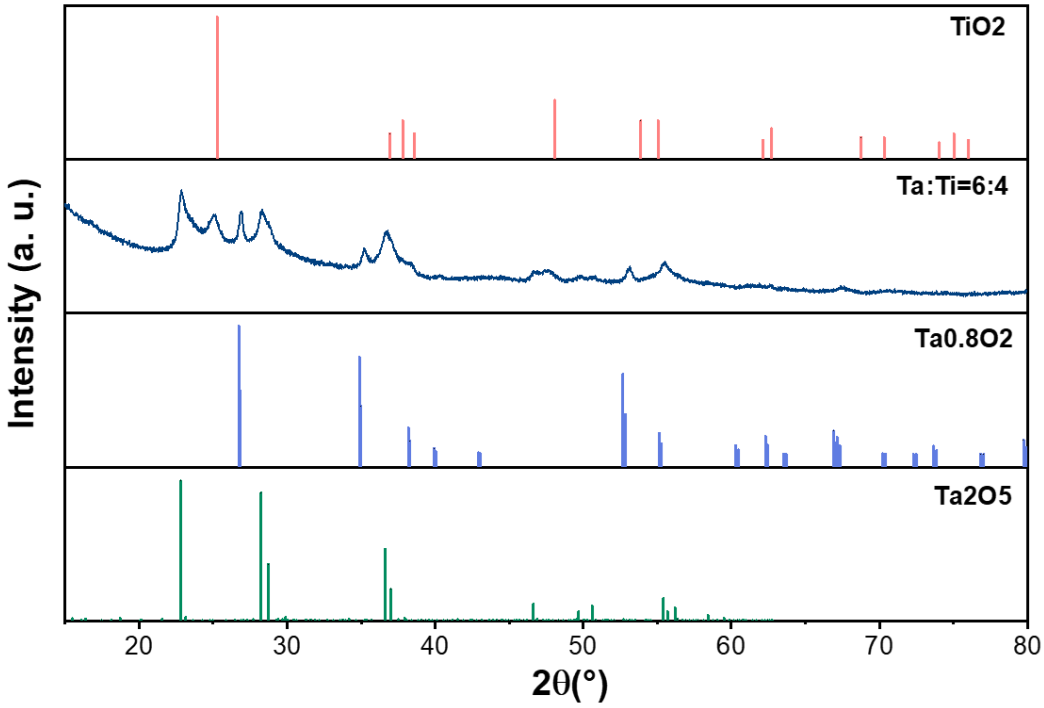

Supplementary Figure 6. XRD pattern of the Ta-TiO_x with a Ta/Ti ratio of 6:4

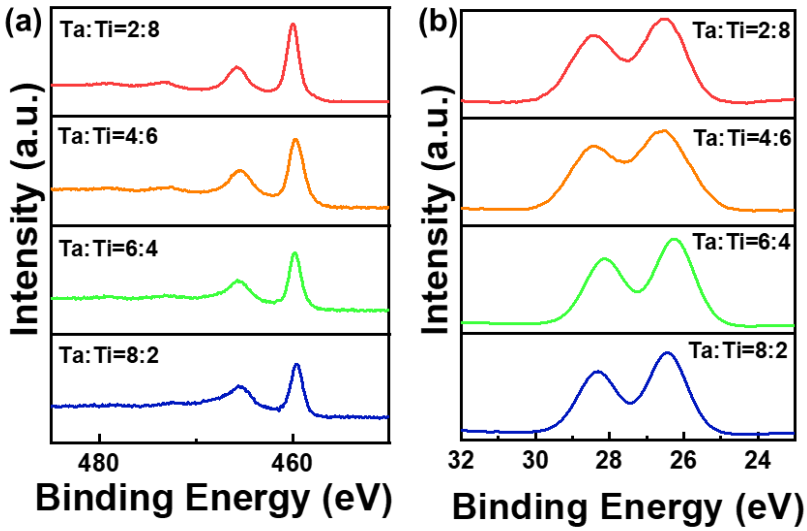

Supplementary Figure 7. The Ti 2p (a) and Ta 4f (b) XPS spectra of the nanoparticles made with different Ta/Ti ratios. The XPS results confirmed no discernable valence change of the Ti and Ta ions as the atomic ratios were varied. The Ta/Ti ratios after synthesis are 2.66:7.34, 4.19:5.81, 6.12:3.88, and 7.21:2.79, respectively. The actual elemental composition ratios of the nanoparticles are close to that of the precursor ratios designed.

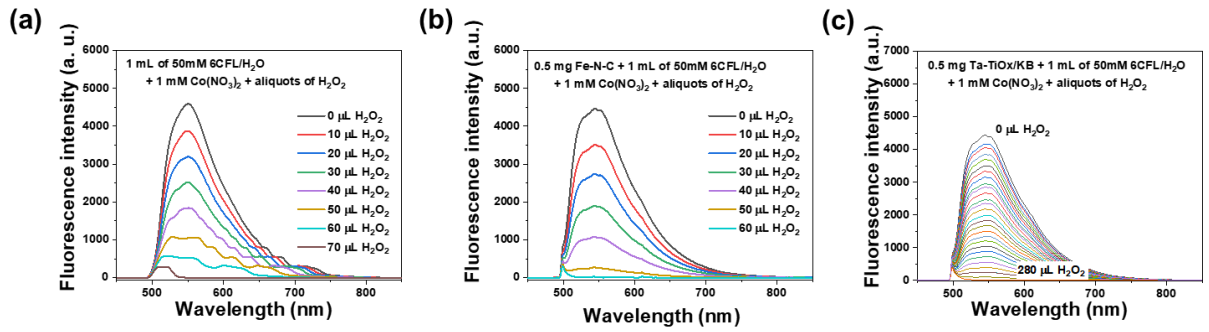

Supplementary Figure 8. Raw Fluorescence spectra obtained in the 6CFL dye solution containing Fenton's reagent and Fe-N-C or Ta-TiO_x/KB as a function of the volume of H_2O_2 added. (a) only Fenton's reagent, (b) Fenton's reagent/Fe-N-C, and (c) Fenton's reagent/Ta-TiO_x scavengers

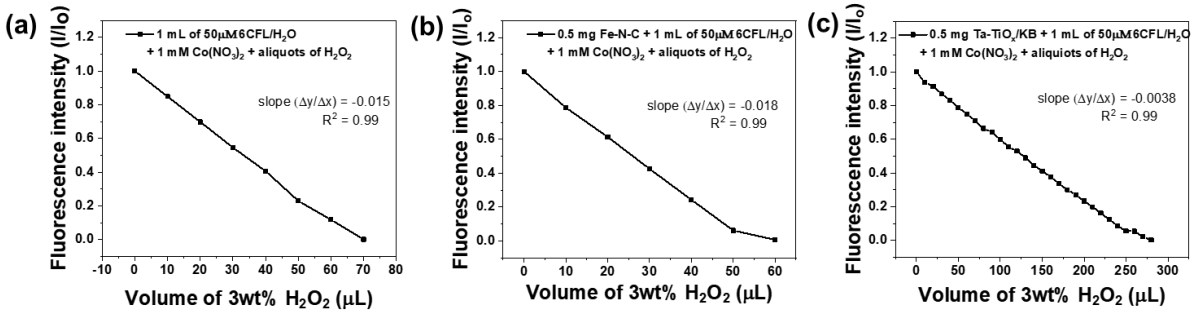

Supplementary Figure 9. Fluorescence intensity decay plots obtained in the 6CFL dye solution containing Fenton's reagent and Fe-N-C or Ta-TiO_x/KB as a function of the volume of H_2O_2 added. (a) only Fenton's reagent, (b) Fenton's reagent/Fe-N-C, and (c) Fenton's reagent/Ta-TiO_x scavengers. The fluorescence intensity is proportional to the overall radical concentration.

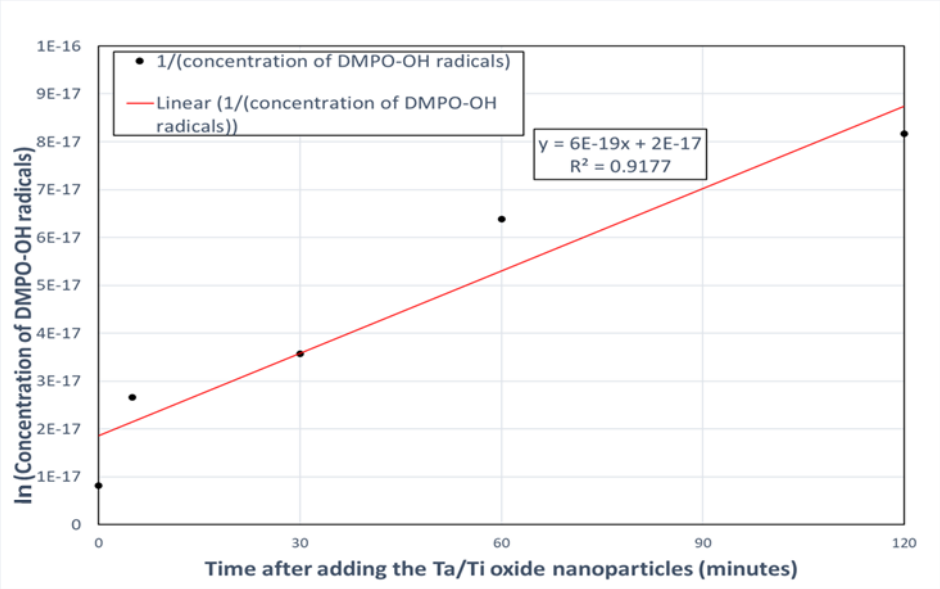

Supplementary Figure 10. The second order fit of the OH-DMPO• radical decay. The low concentration of [OH-DMPO•] in the presence of the Ta-TiO_x radical scavengers well fits a second-order decay.

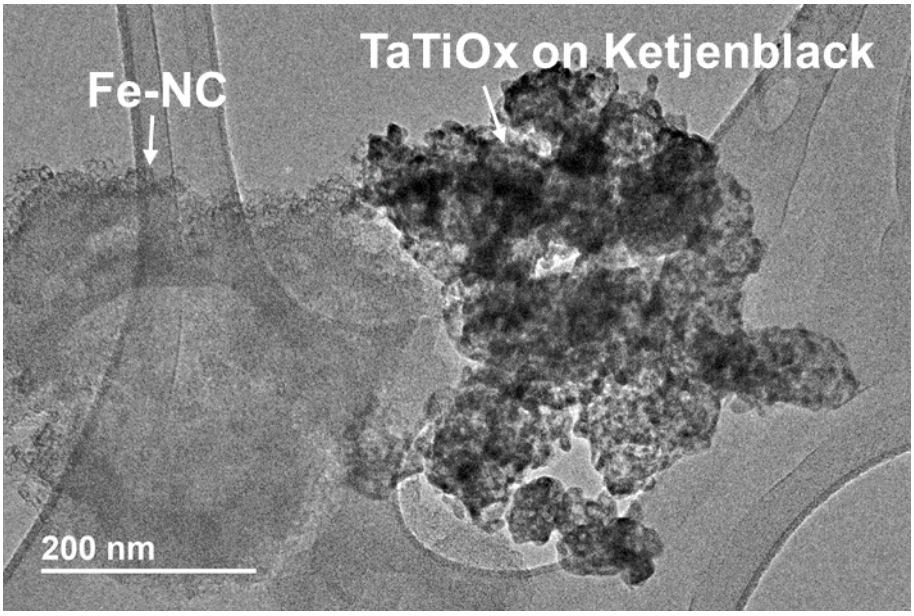

Supplementary Figure 11. TEM image of the Fe-N-C catalyst synthesized from ZIF-8 and the Ta-TiO_x scavenger nanoparticles. The TEM sample was directly diluted from the working electrode ink with 10 wt% nanoparticle scavengers.

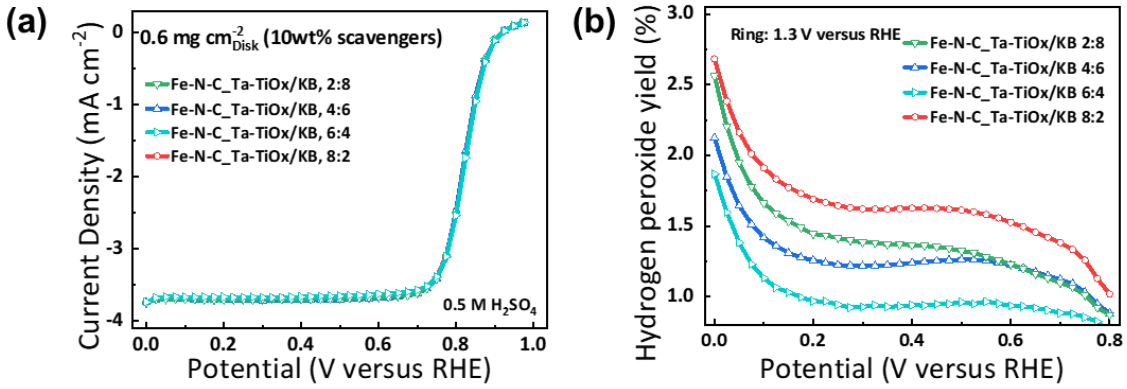

Supplementary Figure 12. Electrocatalytic evaluation of the Ta-TiO_x nanoparticles as H_2O_2 scavengers. (a) The ORR performance of the Fe-N-C catalysts with the Ta-TiO_x nanoparticles at Ta/Ti ratios of 2:8, 4:6, 6:4, and 8:2. The electrocatalytic activity was not influenced by the introduction of the nanoparticles with these Ta/Ti ratios. (b) The H_2O_2 yield of the Fe-N-C catalyst with 10 wt% Ta-TiO_x nanoparticles at Ta/Ti ratios of 2:8, 4:6, 6:4, and 8:2.

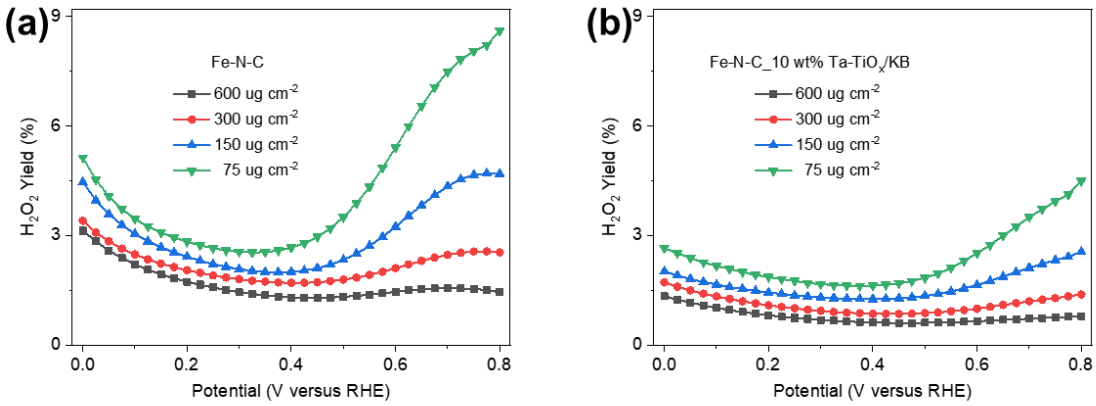

Supplementary Figure 13. RRDE tests to detect the H_2O_2 yield for different Fe-N-C loadings (a) without and (b) with the Ta-TiO_x scavengers.

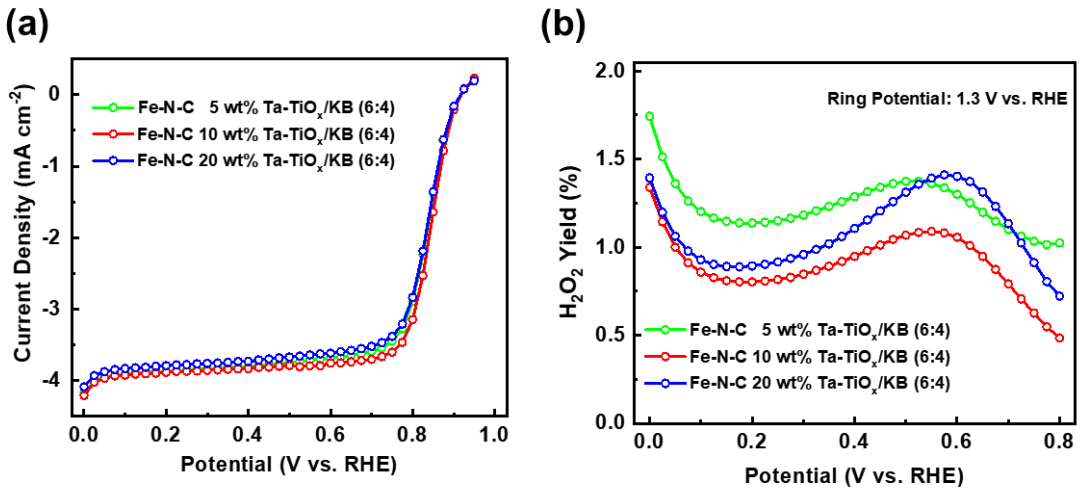

Supplementary Figure 14. The influence of different Ta-TiO_x/KB weight ratios (a) The ORR activity of the Fe-N-C catalyst after adding the Ta-TiO_x/KB at different weight ratios. At 10 wt% Ta-TiO_x/KB, the activity is slightly higher than that with 5 wt% and 20 wt% Ta-TiO_x/KB. (b) The H_2O_2 yield after adding the Ta-TiO_x/KB at different weight ratios. At 10 wt%, the H_2O_2 scavenging performance, with a H_2O_2 yield of less than 1%, is superior compared with that of the 5 wt% and 20 wt% loading.

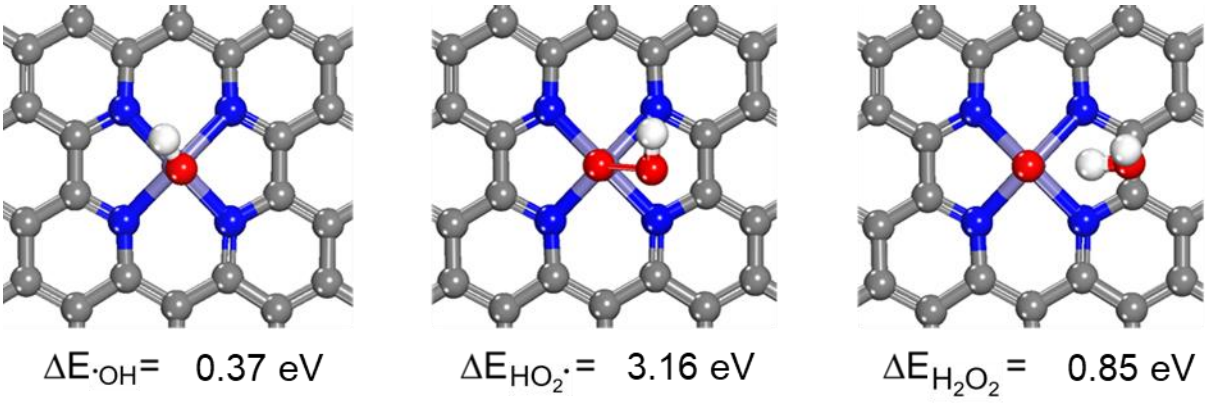

Supplementary Figure 15. Top-down views of the preferred binding sites of the Fe-N-C catalyst for ·OH(left), HO_2·(middle), and H_2O_2(right) radicals and their calculated adsorption energies. The grey, blue, cyan, red and white balls represent C, N, Fe, O and H atoms, respectively.

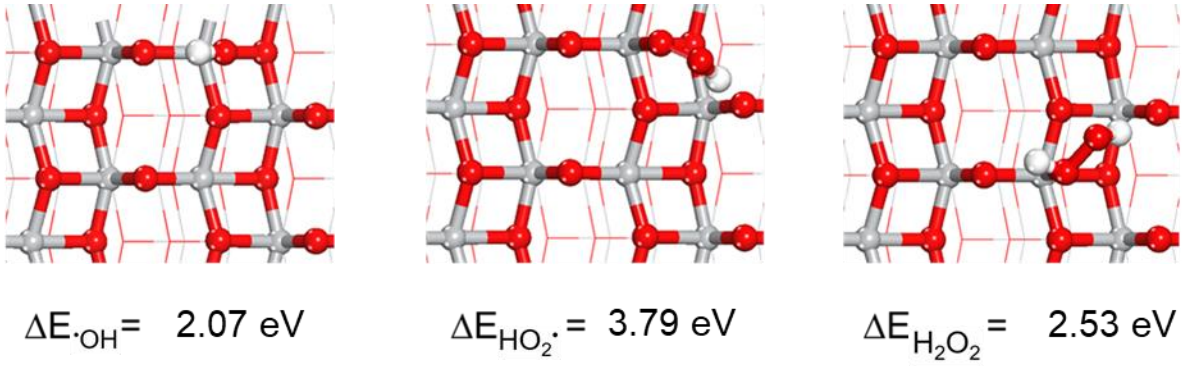

Supplementary Figure 16. Top-down views of the preferred binding sites of the TiO_2 (101) surface for ·OH(left), HO_2·(middle), and H_2O_2(right) radicals and their calculated adsorption energies. The grey, red and white balls represent Ti, O and H atoms, respectively.

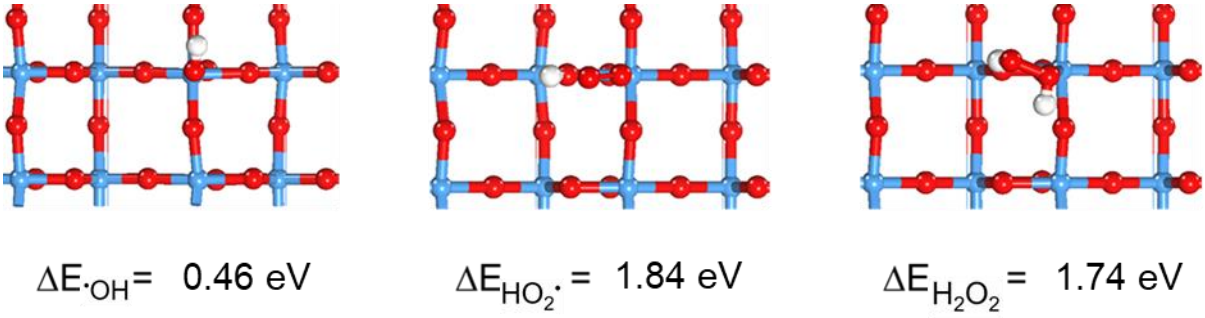

Supplementary Figure 17. Top-down views of the preferred binding sites of the Ta_2O_5 (100) surface for ·OH(left), HO_2·(middle), and H_2O_2(right) radicals and their calculated adsorption energies. The cyan, red and white balls represent Ta, O and H atoms, respectively.

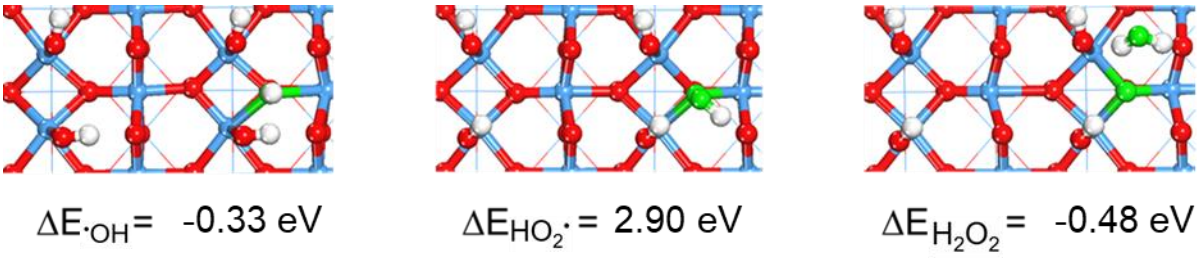

Supplementary Figure 18. Top-down views of the preferred binding sites of the TaO_2-OH (110) surface for ·OH(left), HO_2·(middle), and H_2O_2(right) radicals and their calculated adsorption energies. The cyan and red balls represent Ta and O atoms in TaO_2-OH; The green and white balls represent O and H atoms in radicals.

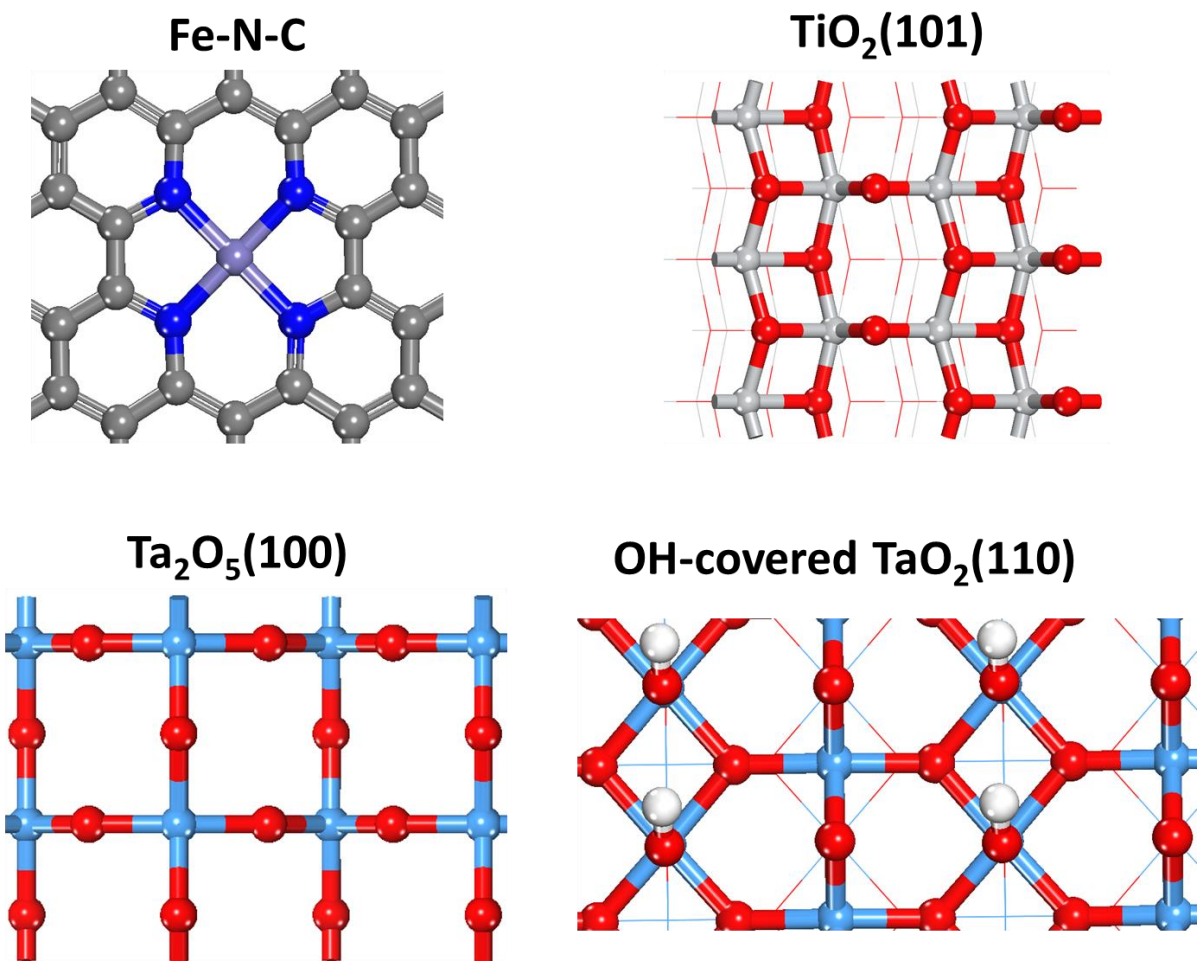

Supplementary Figure 19. The lattice structure of the different surfaces for the DFT calculations.

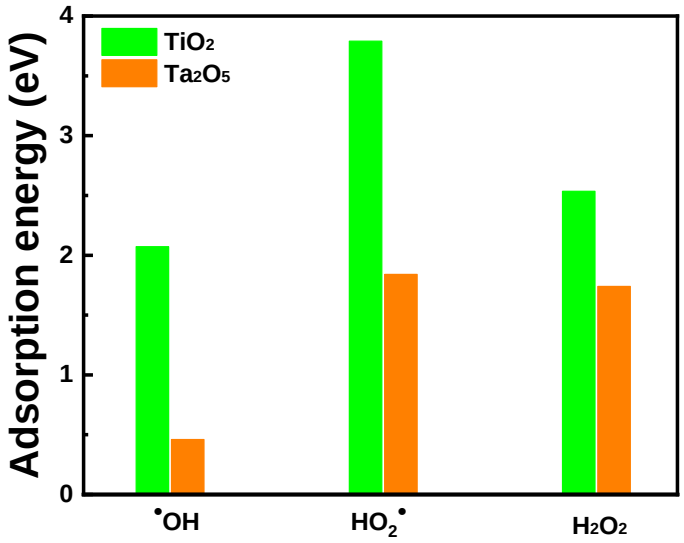

Supplementary Figure 20. Adsorption energies of H_2O_2 and related radicals on TiO_2 and Ta_2O_5 surfaces

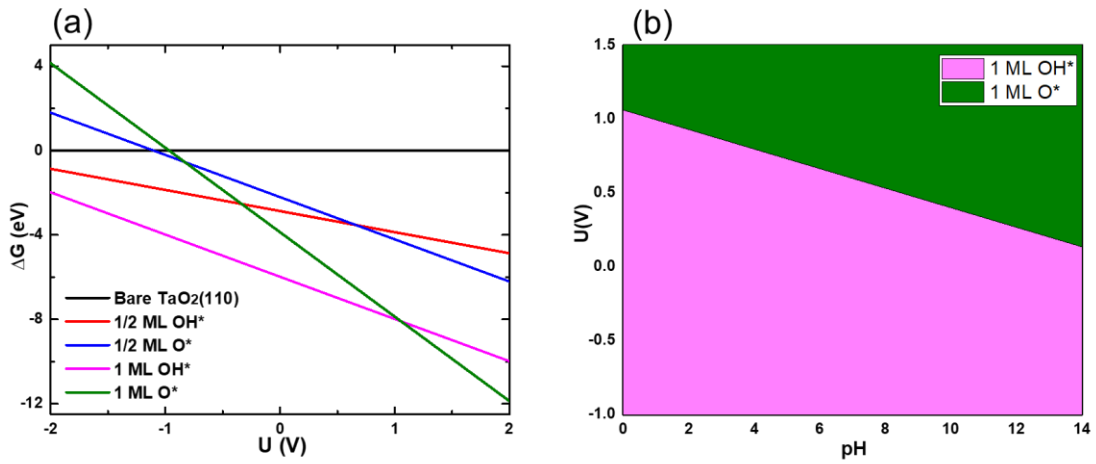

Supplementary Figure 21. Stability analysis (a) Stability of OH* and O* on TaO_2(110) at pH = 0. (b) Surface Pourbaix diagram for TaO_2(110). We use an OH pre-adsorbed TaO_2(110) surface for the investigations of the catalytic mechanisms of H_2O_2 decomposition. To assess the stability of this surface under the reaction conditions, we have constructed the Pourbaix diagram using the concept of the theoretical standard hydrogen electrode (SHE)[4]. It is assumed the surface is in equilibrium with protons and liquid water at 298 K, so that oxygen and hydroxyl may be exchanged between the surface and a reference electrolyte through the steps of $H_2O(l) + * \leftrightarrow HO* + H^+(aq) + e^-$ and $HO* \leftrightarrow O* + H^+(aq) + e^-$. From this method, the free energy of a given surface structure can be calculated as a function of the potential U_{SHE} and pH. We consider the following surface structures of TaO_2(110): 1/2 ML OH*, 1/2 ML O*, 1 ML OH*, 1ML O*, and the bare surface. The lowest line determines the surface with the lowest free energy at a given potential. The surface Pourbaix diagram is then constructed by plotting the most stable surface as a function of the pH and U_{SHE}. As one can see, under the reaction conditions (pH = 0 and U = 0.8 ~ 0.9 V), the TaO_2(110) surface with 1 ML OH* is the most stable. At potentials above 1.06 V, the adsorbed OH* is further oxidized to O*, and 1 ML O* becomes the most stable surface.

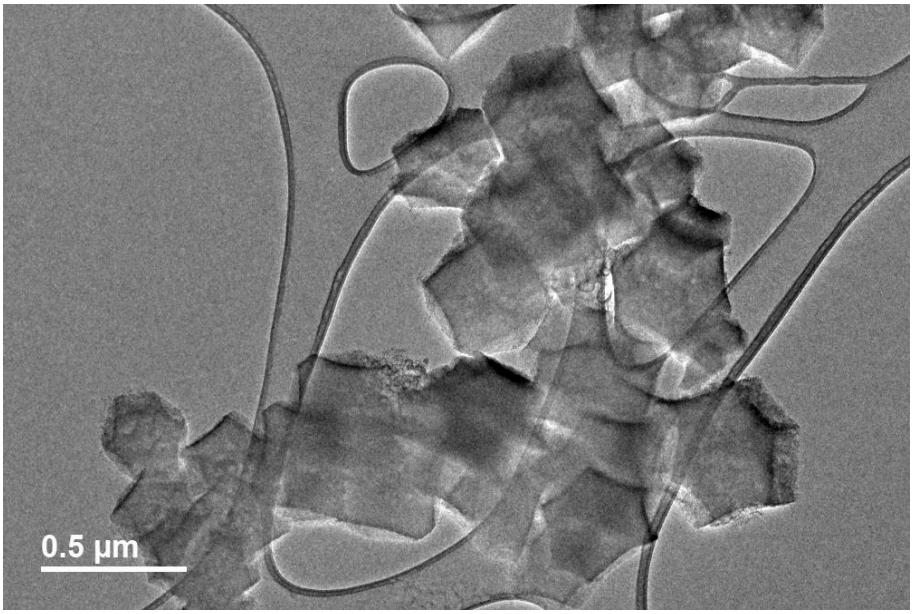

Supplementary Figure 22. TEM image to show the morphology of the Fe-N-C catalyst synthesized from ZIF-8.

Supplementary Table

Supplementary Table 1. The calculated electronic energies (eV) to compute $OH/HO_2/H_2O_2$ binding energies on Fe-N-C, TaO_2-OH, TiO_2 and Ta_2O_5. The $\Delta E(^{\bullet}OH)$ was computed by using $\Delta E_{^{\bullet}OH} = E_{*OH} - E_{slab} - (E_{H2O} - 1/2E_{H2}) = E_{*OH} - E_{slab} - [(-14.22\ eV) - 1/2*(-6.76\ eV)] = E_{*OH} - E_{slab} - (-10.84\ eV)$. The $\Delta E(HO_2^{\bullet})$ was computed by using $\Delta E_{HO2^{\bullet}} = E_{*OOH} - E_{slab} - (2E_{H2O} - 3/2E_{H2}) = E_{*OOH} - E_{slab} - [2*(-14.22\ eV) - 3/2*(-6.76\ eV)] = E_{*OH} - E_{slab} - (-18.30\ eV)$. The $\Delta E(H_2O_2)$ was computed by using $\Delta E_{H2O2} = E_{*H2O2} - E_{slab} - (2E_{H2O} - E_{H2}) = E_{*H2O2} - E_{slab} - [2*(-14.22\ eV) - (-6.76\ eV)] = E_{*H2O2} - E_{slab} - (-21.68\ eV)$.

	FeNC	**TaO_2-OH**	**TiO_2**	**Ta_2O_5**
Slab	-540.66	-356.55	-561.84	-743.81
Slab + OH*	-551.14	-367.72	-570.62	-754.19
$\Delta E(^{\bullet}OH)$	**0.37**	**-0.33**	**2.07**	**0.46**
Slab + OOH*	-555.81	-371.95	-576.35	-760.26
$\Delta E(HO_2^{\bullet})$	**3.16**	**2.90**	**3.79**	**1.84**
Slab + H_2O_2*	-561.50	-378.72	-581.00	-763.75
$\Delta E(H_2O_2)$	**0.85**	**-0.48**	**2.53**	**1.74**

Supplementary References

1. Henglein, A. J. W. T. Spinks. R. J. Woods: An Introduction to Radiation Chemistry, Third Edition, John-Wiley and Sons, Inc., New York, Toronto 1990. ISBN 0-471-61403-3. 574 Seiten, Preis: DM 91, 45. *Berichte der Bunsengesellschaft für Phys. Chemie* **95**, 451–451 (1991).

2. Czapski, G. & Bielski, B. H. J. The Formation and Decay of H2O3 And HO2 in Electron-Irradiated Aqueous Solutions 1. *J. Phys. Chem.* **67**, 2180–2184 (1963).

3. Mulcahy, M. F. R. & Young, B. C. The reaction of hydroxyl radicals with carbon at 298 K. *Carbon N. Y.* **13**, 115–124 (1975).

4. Russell, A. E. Electrocatalysis: Theory and experiment at the interface. *Phys. Chem. Chem. Phys.* **10**, 3607–3608 (2008).